Supporting Information

Lithium Deposition-Induced Fracture of Carbon Nanotubules and Its Implication to Solid-State Batteries

Jingzhao Chen[†], Chao Zhao[§], Dingchuan Xue[‡], Liqiang Zhang[†], Tingting Yang[†], Congcong Du[†], Xuedong Zhang[¢], Ruyue Fang[‡,±], Baiyu Guo[†], Hongjun Ye[†], Hui Li[†], Qiushi Dai[†], Jun Zhao[†], Yanshuai Li[†], Stephen J. Harris[€], Yongfu Tang[†,£,], Feng Ding[§,*], Sulin Zhang[‡,*], Jianyu Huang[†,¢,*]*

[†]Clean Nano Energy Center, State Key Laboratory of Metastable Materials Science and Technology, Yanshan University, Qinhuangdao 066004, P. R. China.

[§]Center for Multidimensional Carbon Materials, Institute for Basic Science (IBS), School of Materials Science and Engineering, Ulsan National Institute of Science and Technology (UNIST), Ulsan 44919, Republic of Korea.

[‡]Department of Engineering Science and Mechanics, The Pennsylvania State University, University Park, PA 16802, USA.

[£]Hebei Key Laboratory of Applied Chemistry, College of Environmental and Chemical Engineering, Yanshan University, Qinhuangdao 066004, P.R. China.

[±]Department of Materials Science and Engineering, The Pennsylvania State University, University Park, PA 16802, USA.

[€]Energy Storage Division, Lawrence Berkeley, National Laboratory, Berkeley, CA 94720, USA.

[¢]School of Materials Science and Engineering, Xiangtan University, Xiangtan, Hunan 411105, P. R. China.

Corresponding Authors

*Correspondence to: jyhuang8@hotmail.com; suz10@psu.edu; f.ding@unist.ac.kr; tangyongfu@ysu.edu.cn.

Supporting Methods

(1) The preparation of hollow CNT

The hollow CNT was fabricated through a typical chemical vapor deposition method. Anodic aluminum oxide (AAO) membranes with pore size about 200 nm were first placed in a tube furnace. After that, they were heated in an argon (Ar) atmosphere up to 700 °C to deposit a carbon layer (~24 nm) via C_3H_6 decomposition at an atmospheric pressure. The carbon-coated AAO membranes were etched away with 10% hydrofluoric acid (HF) and then washed with deionized water several times. The final products were dried at 60 ℃ in vacuum. A bulk dry CNT was ultrasonically dispersed in ethanol and then dropped onto a clean glass slide with a half-copper mesh and dried in a furnace.[1, 2]

(2) The nanobattery setup for in situ TEM observation

The nanobattery consists of a bulk Li_2O or Li_2CO_3 coated-Li metal as anode, the Li_2O or Li_2CO_3 layer on the surface of Li metal as the solid electrolyte, and the CNTs attached to the half copper mesh as the counter electrode (**Figures S1 and S2**). The Li anode was driven to contact with a single hollow CNT via the piezoceramic controlled manipulator in a 1 mbar CO_2 atmosphere or in vacuum, and a negative potential was applied to the CNT electrode to initiate lithiation and lithium deposition. Li was deposited in the hollow CNT in the CO_2 ambient after the CNT was fully lithiated. The Li_2CO_3 electrolyte covered on the bulk Li anode is stable and does not decompose under our experimental conditions.

(3) The compression and tensile experiments

In order to measure the mechanical strength of CNT prior to and after lithiation, we created a home-made ETEM-AFM device (**Figure S9**) to characterize their mechanical properties. The AFM tips were purchased from Burker Company with a stiffness of k=40 N/m. As the beam length (520 μm) is much larger than the deflection of cantilever (< 5 μm), a linear relationship between dx (displacement of the AFM tip) and P (force applied on the whisker) was assumed.[3] The compressive or tensile strength of CNT was

calculated by measuring the deflection of the cantilever beam in a high magnification transmission electron microscope image.

In the compression experiments of pristine and lithiated CNTs from the radial direction (corresponding schematic and TEM image in **Figure S9a, b**), we first touched the CNTs by a tip-flattened aluminum (Al) rod, which was mounted onto the other end of the TEM-STM holder (Pico Femto FE-F20). And a Si AFM cantilever beam attached to an Al rod with conductive silver epoxy (with the effective spring stiffness $k = 40$ N/m) was installed on the counter side of sample holder. During the compression tests, a beam blocking bar was inserted into the field of view as the reference for displacement and force measurements reference. The flattened AFM tip was shaped by focus ion beam. The pristine and lithiated CNTs was pushed upward by piezoelectric tube of the holder, which pushed up the AFM tip, thus permitting real-time measurements of the stress generated in pristine or lithiated CNTs. In addition to the compression experiments by the ETEM-AFM platform, radial compression tests of the pristine CNTs was also carried out in a Hysitron PI95 sample holder system.

In the tensile test of the pristine or lithiated CNTs from the longitudinal direction (corresponding schematic and TEM image in **Figure S9c, d**), the pristine and lithiated CNTs were welded on the AFM tip by the ionic liquid ($AlCl_3$ was slowly dissolved in imidazole with the mass ratio of 1.3:1, until the light yellow and transparent ionic liquid was stirred in the glovebox for several minutes.) under e-beam solidification in ETEM.

The detailed information of the tensile test setup is descried as the following. First, ionic liquid (IL) and the pristine CNTs were placed on two sides of a flattened Al rod, (**Figure S17a**). Second, the IL was driven to contact the AFM tip when the IL wetted the AFM tip, afterwards the AFM and the Al rod was separated, leaving some IL on the AFM tip for welding the pristine or lithiated CNT (**Figure S17b**). Third, the pristine or lithiated CNT was manipulated to contact with the IL coated AFM tip, and the IL was solidified by e-beam irradiation in ETEM (**Figure S17c**). The CNT was welded to the Al rod in a a similar manner as it was weld to the AFM tip (**Figure S17d**).

Once the contacts were established, the pristine and lithiated CNTs were pulled downward by piezoelectric tube of the TEM-STM sample holder, thus permitting real-time measurements of the stress generated in the pristine/lithiated CNTs. The compressive or tensile force (P) the pristine/lithiated CNTs was calculated by

measuring the deflection of the cantilever beam in high magnification TEM images. As the diameter and the cross-sectional area A of the pristine/lithiated CNTs were measured through in situ TEM imaging, the axial tensile stress, σ, generated in the pristine/lithiated CNTs were determined by $\sigma = P/A$.

(4) FEA Modeling

All finite element analyses were performed using Abaqus to capture the critical yield stress. According to the experimental samples, several full 3D nano hollow cylinder models were built (**Figure S18**). **Figure S18 (a, c)** and **(b, d)** represent the pristine and lithiated CNTs compressed by different AFM tips, respectively. The pristine and lithiated CNTs were fine-meshed with solid elements. Both the AFM tips and the substrate were considered to be rigid, and the shell element was adopted. Then, the center cross-section along yz plane and the cross-section in xz plane were fixed to avoid the CNTs shifting along x-direction and y-direction, respectively. The friction coefficient at the AFM tips/CNT and the CNT/substrate contacts were taken to be 0.02.[4, 5] The Young's moduli are determined from experimental results, and the Poisson's ratio was adopted from literature.[4, 5] Finally, a displacement loading was applied to the different AFM tips, and the force versus displacement and maximum tensile stress versus displacement curves were obtained.

(5) The maximum pressure estimation of lithiated CNTs

Based on the experimental observation, the amorphous CNTs could burst with lithium deposition. Herein, a very simple analytical model was proposed to estimate the bursting pressure. We considered the homogeneous hollow CNT model with a length L, an inner radius r, and an outer radius R. An infinitely small length (dy) of the CNT was selected for force analysis, shown in **Figure S19**. The system is subjected to two types of forces: one is due to the hoop stress (σ), and another one is caused by the internal pressure (P). The amorphous CNT can burst only when the following force equilibrium of the hoop stress and internal pressure were satisfied,

$$\sigma[2(R-r)dy] - P(2rdy) = 0.$$

Finally, the relationship between internal pressure and hoop stress was established via the following formula,

$$P = \sigma \frac{R - r}{r}$$

In the tensile test, the tensile strength of a lithiated CNT with an outer diameter of 283 nm and a thickness of 29.5 nm was measured to be 930 MPa, and the maximum pressure was estimated to be 247 MPa using the above equation. Besides, two CNTs with an outer diameter of 361 nm, a thicknesses of 71 nm and 46 nm were considered for indentation tests. Based on the FEA simulations, the maximum hoop and axial stresses were calculated. We take the higher stress of them as the estimated strength: one is 1840 MPa (**Figure 3t**), and another one is 2000 ~ 2530 MPa (**Figure S12t**), thus the maximum pressure inside the CNTs are estimated to be 1193.1 and 684.0 ~ 865.3 MPa, respectively.

Supporting Movies

Description of Movie S1

An in situ TEM movie showing the lithium deposition from the radial direction of CNT in a 1 mbar CO_2 ambient (corresponding to **Figure S2a-e**). the movie was recorded at 5 frames/second in TEM bright field images, and played at 193× speed.

Description of Movie S2

An in situ TEM movie showing the fracture of CNT induced by lithium deposition in a CO_2 ambient (corresponding to **Figure 1a-i**). The movie was recorded at 5 frames/second in TEM bright field images, and played at 48× speed.

Description of Movie S3

An in situ TEM movie showing the fracture of CNT induced by lithium deposition in a CO_2 ambient (corresponding to **Figure 1j-p**). The movie was recorded at 5 frames/second in TEM bright field images, and played at 115× speed.

Description of Movie S4

An in situ TEM movie showing the fracture of CNT induced by lithium deposition in a CO_2 ambient (corresponding to **Figure S6a-h**). The movie was recorded at 5 frames/second in TEM bright field images, and played at 89.5× speed.

Description of Movie S5

An in situ TEM movie showing the fracture of CNT induced by lithium deposition in a CO_2 ambient (corresponding to **Figure S6i-o**). The movie was recorded at 5 frames/second in TEM bright field images, and played at 25× speed.

Description of Movie S6

An in situ TEM movie showing the lithium deposition from the longitudinal direction of CNT in vacuum (corresponding to **Figure S8a-e**). The movie was recorded at 5 frames/second in TEM bright field images, and played at 45× speed.

Description of Movie S7

An in situ TEM movie showing the nanowelding of the pristine CNT by ionic liquid and tensile experiment of the pristine CNT (corresponding to **Figure 2a-h**). The movie was recorded at 5 frames/second in TEM bright field images, and played at 142× speed.

Description of Movie S8

An in situ TEM movie showing the nanowelding of a lithiated CNT by ionic liquid and tensile experiment of the lithiated CNT (corresponding to **Figure 2l-q**). The movie was recorded at 5 frames/second in TEM bright field images, and played at 140× speed.

Description of Movie S9

An in situ TEM movie showing the nanowelding of a pristine CNT by ionic liquid and tensile experiment of the pristine CNT (corresponding to **Fiure S10a-i**). The movie was recorded at 5 frames/second in TEM bright field images, and played at 4× speed.

Description of Movie S10

An in situ TEM movie showing the nanowelding of a lithiated CNT by ionic liquid and tensile experiment of the lithiated CNT (corresponding to **Figure S10l-r**). The movie was recorded at 5 frames/second in TEM bright field images, and played at 90× speed.

Description of Movie S11

An in situ TEM movie showing the compression experiment of the pristine CNT from the radial direction via the Hysitron PI95 sample holder system (corresponding to **Fiures 3a-f and S11a-o**). The movie was recorded at 5 frames/second in TEM bright field images, and played at 9× speed.

Description of Movie S12

An in situ TEM movie showing the compression experiment of the lithiated CNT from the radial direction (corresponding to **Figure 3g-l**). The movie was recorded at 5 frames/second in TEM bright field images, and played at 44× speed.

Description of Movie S13

An in situ TEM movie showing the compression experiment of a pristine CNT from

the radial direction (corresponding to **Figure S12a-f**). The movie was recorded at 5 frames/second in TEM bright field images, and played at 9× speed.

Description of Movie S14

An in situ TEM movie showing the compression experiment of a lithiated CNT from the radial direction (corresponding to **Figures S12g-l and S13a-j**). The movie was recorded at 5 frames/second in TEM bright field images, and played at 154× speed.

Supporting Figures

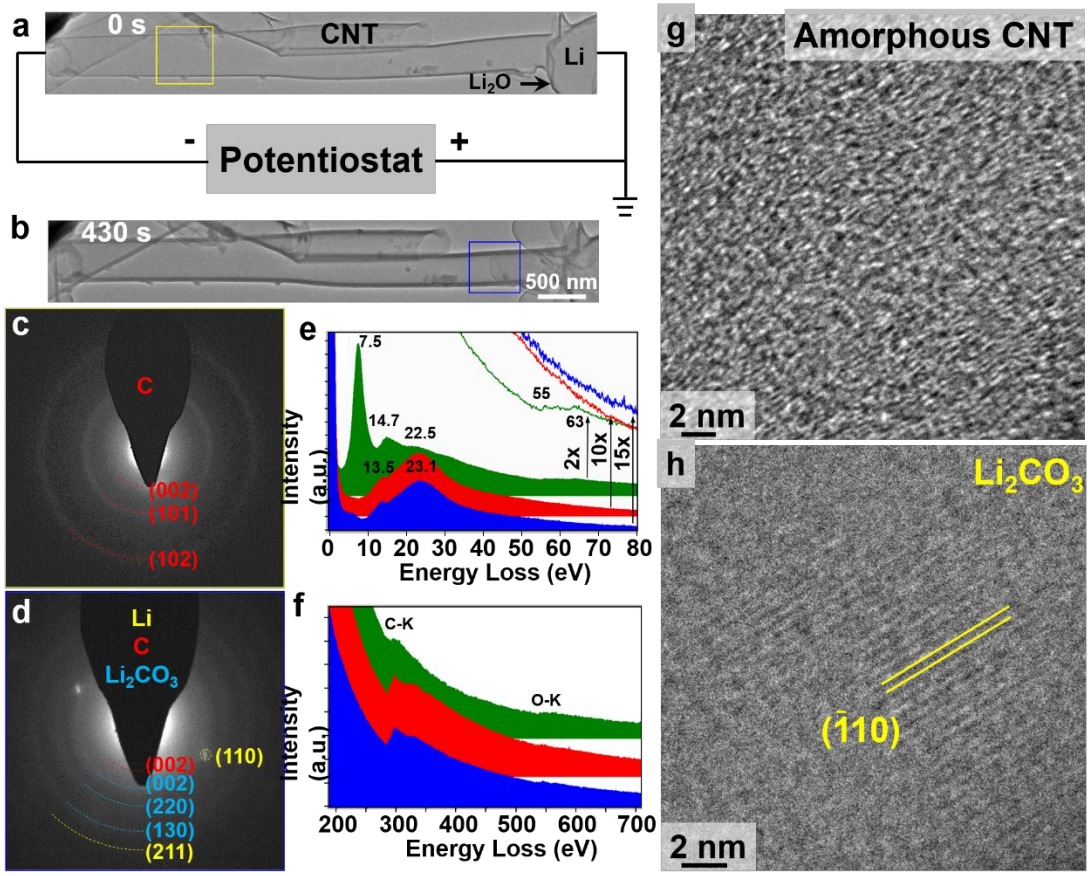

Figure S1. The nanobattery setup and characterizations of the pristine and lithiated CNTs. (a) The nanobattery setup. (b) A TEM image of the lithiated CNT. (c, d) SAED patterns of the pristine and lithiated CNTs, respectively. (e, f) Low-loss and core-loss spectra of the deposited lithium (red), the pristine (green) and lithiated (blue) CNTs, respectively. (g, h) HRTEM images of the pristine and lithiated CNTs, respectively.

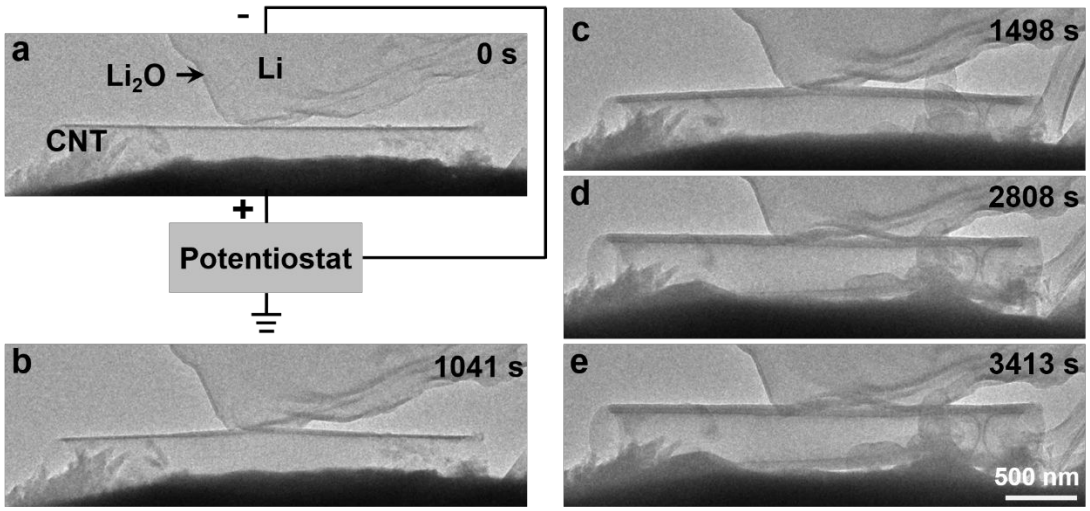

Figure S2. Lithiation of CNT from radial direction. (a) The nanobattery setup. (b-e) Sequential TEM images of the lithiation process of a CNT.

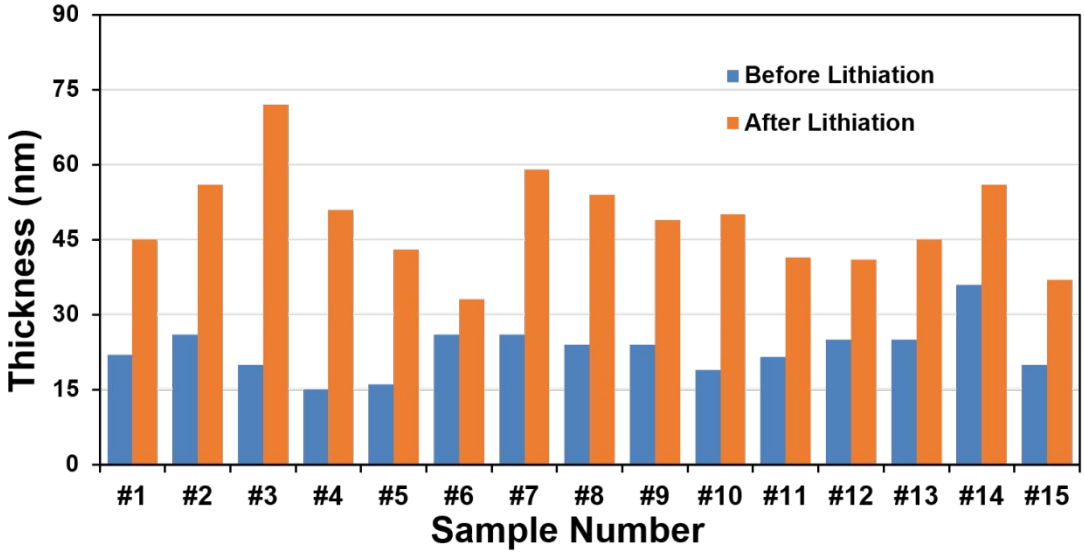

Figure S3. Thickness of the CNT walls before (blue) and after (orange) lithiation.

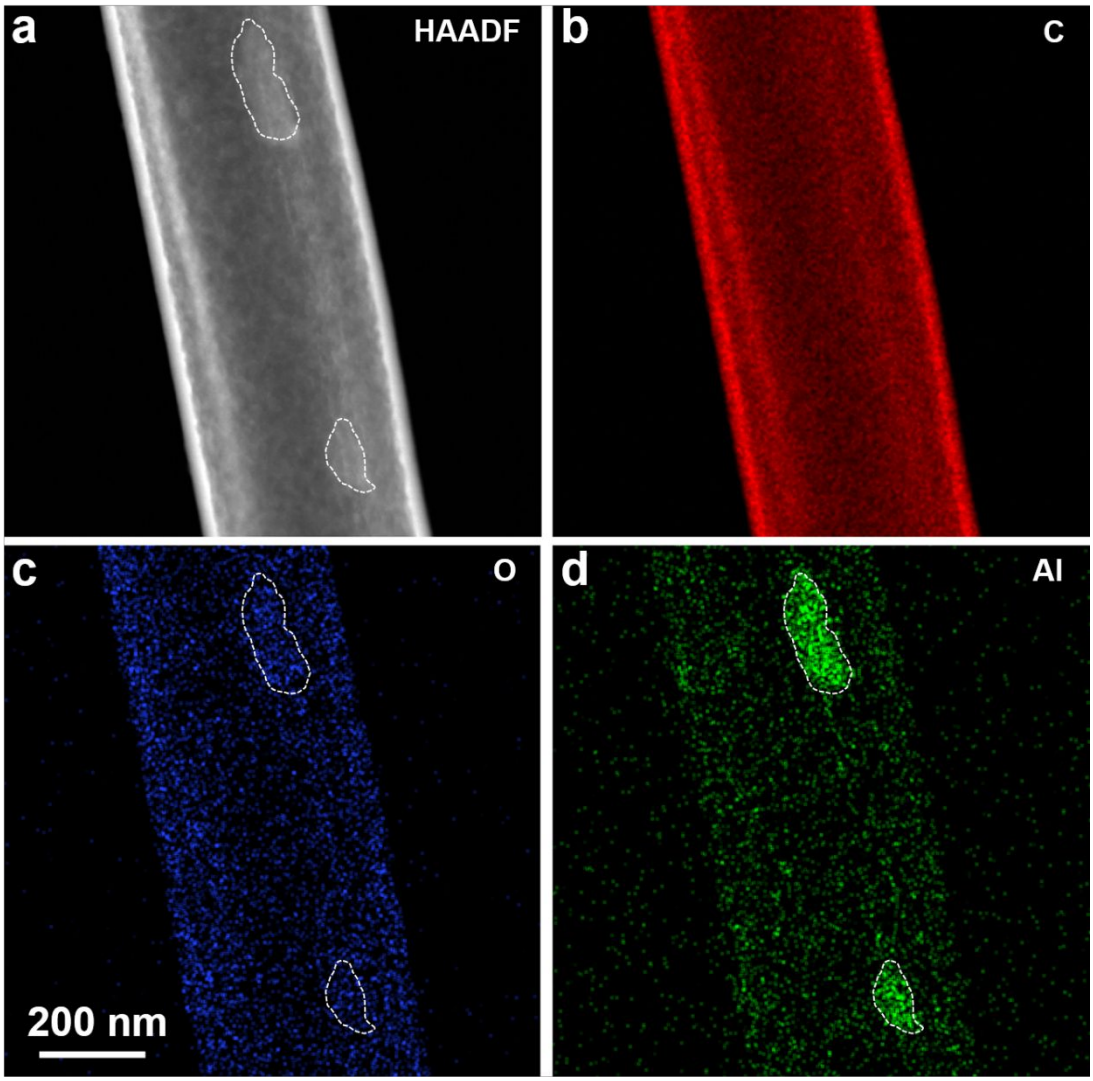

Figure S4. (a) A HAADF image of a pristine CNT. (b-d) Elemental mapping of the CNT, showing Al_2O_3 nanoparticles inside the CNT.

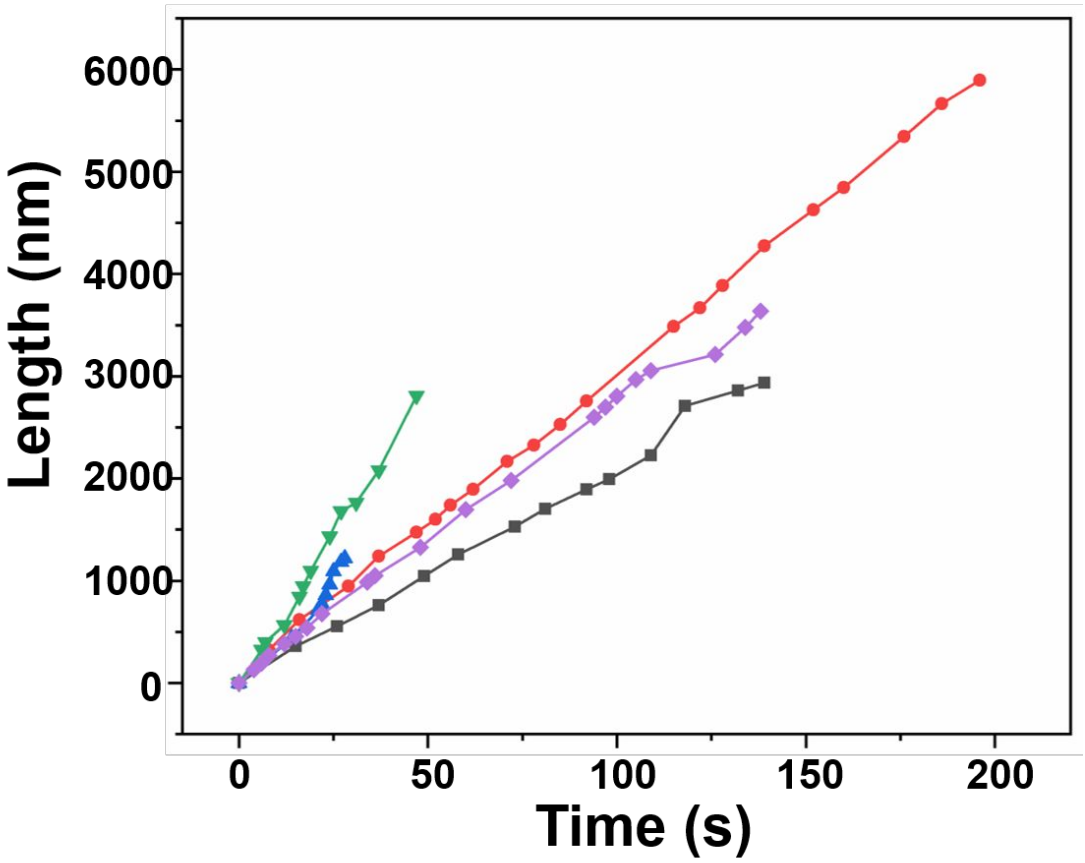

Figure S5. Lithium growth length vs time plot.

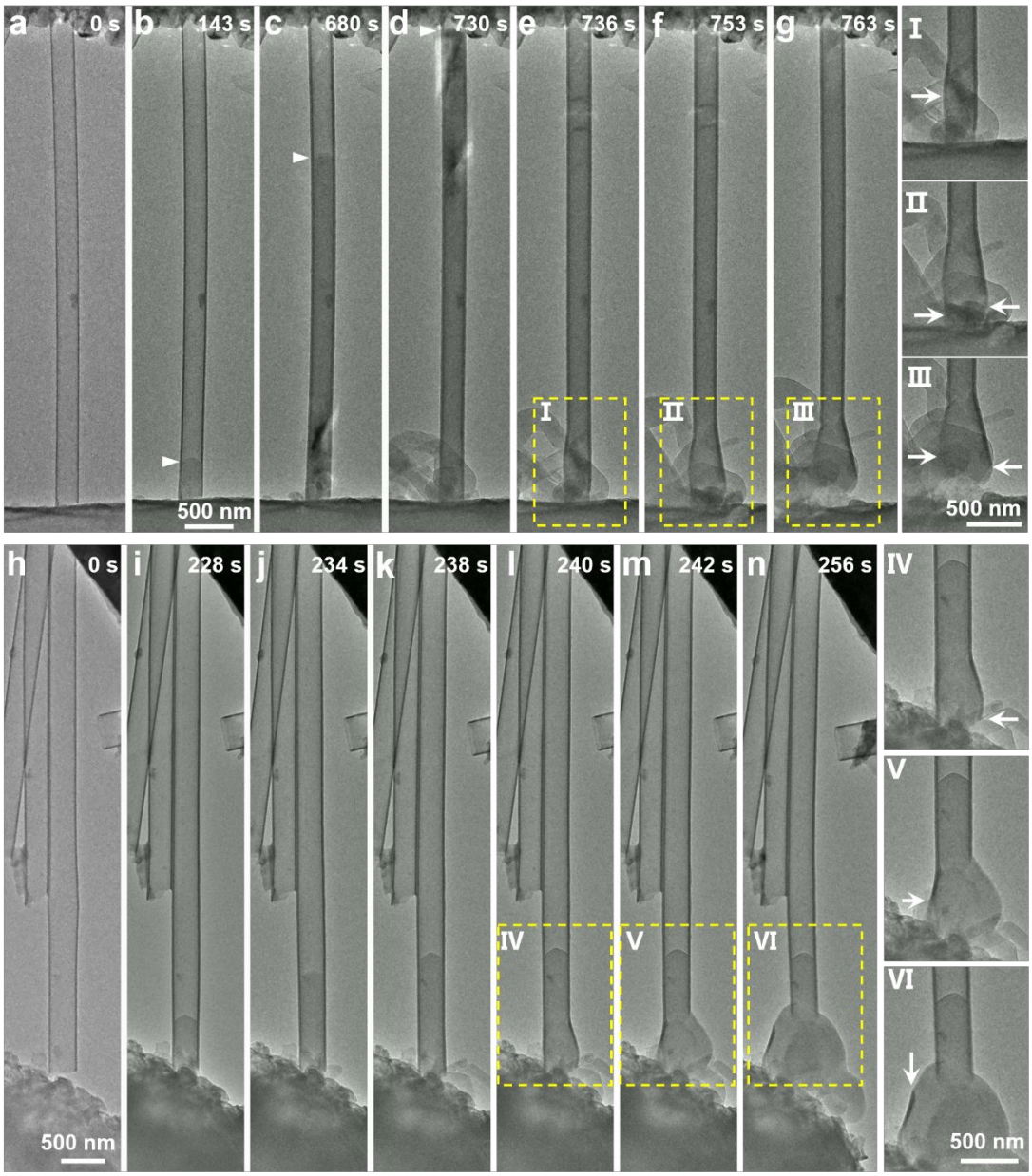

Figure S6. Two sets of time-lapse TEM images (a-g, h-n) showing the fracture of CNTs induced by lithium deposition in a CO_2 ambient. The applied voltage was -1.4 V in (a-g) and -0.8 V in (h-n). "I" to "III" and "IV" to "VI" are local magnification of boxed regions in "(e)" to "(g)" and "(i)" to "(n)", respectively, showing the fracture of the CNTs. Arrowheads point out the lithium deposition fronts. White arrows point out the fracture location of the CNT walls.

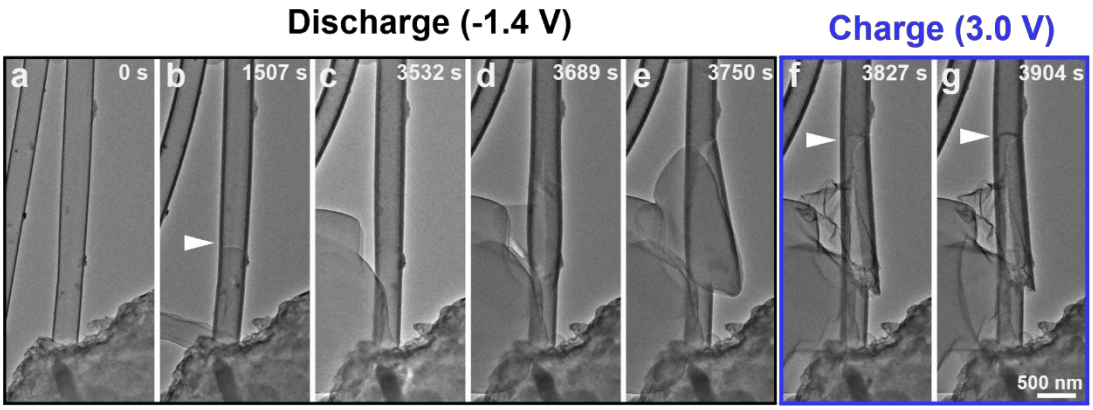

Figure S7. Time lapse TEM images of Li deposition and stripping inside a single hollow CNT. (a-e) Li deposition. When a potential of -1.4 V was applied, Li was deposited in the CNT following the lithiation of the CNT. (f, g) Li stripping. When the potential was reversed, Li was stripped away (white arrowhead). However, the fractured CNT cannot be recovered to initial shape.

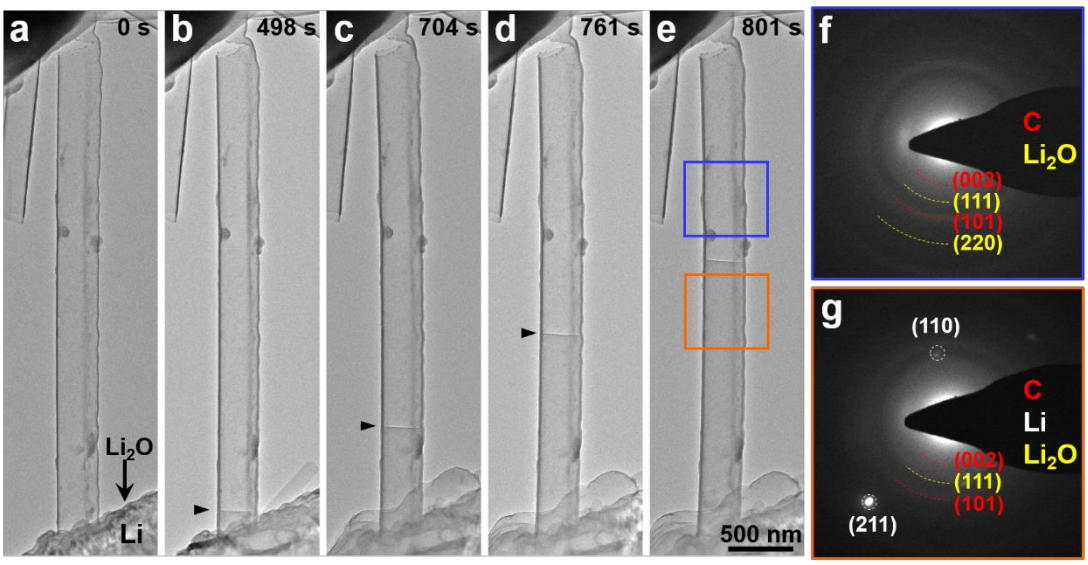

Figure S8. Time lapse TEM images showing lithium deposition inside CNT in vacuum. A negative potential was applied in CNT electrode to initial the lithiation of CNT and lithium deposition (a-e). Arrowheads point out the lithium deposition fronts. A flat front inside lithiated CNT was observed during the lithium deposition. (f, g) SAED patterns showing tow location of the lithiated CNT and Li deposition inside CNT, which are indexed as C, Li and Li_2O.

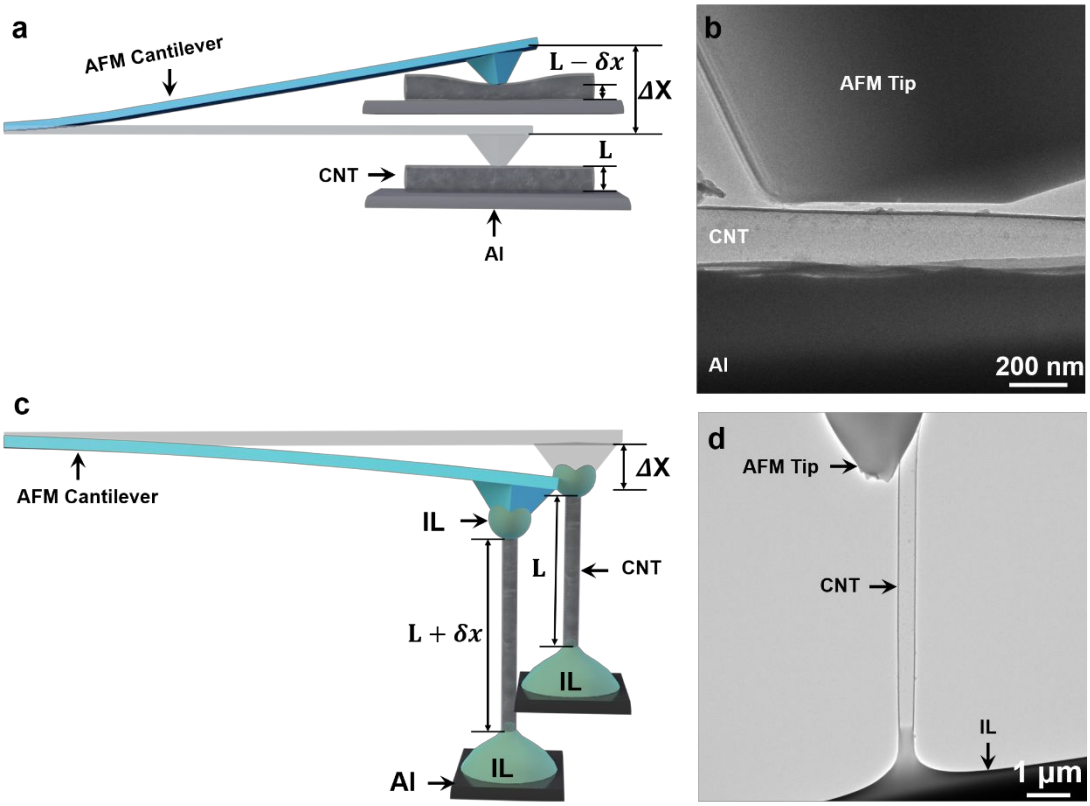

Figure S9. Schematic of ETEM-AFM platform used for compression or tensile tests of the pristine/lithiated CNTs (a, c). TEM images showing the compression of a pristine CNT from the radial Direction (b), and the tensile experiment of a pristine CNT from the longitudinal direction (d). The pristine/lithaited CNTs were welded on the AFM tip by e-beam solidification of ionic liquid (IL) in ETEM. The IL consists of imidazole and $AlCl_3$ with a mas ratio of 1:1.3.

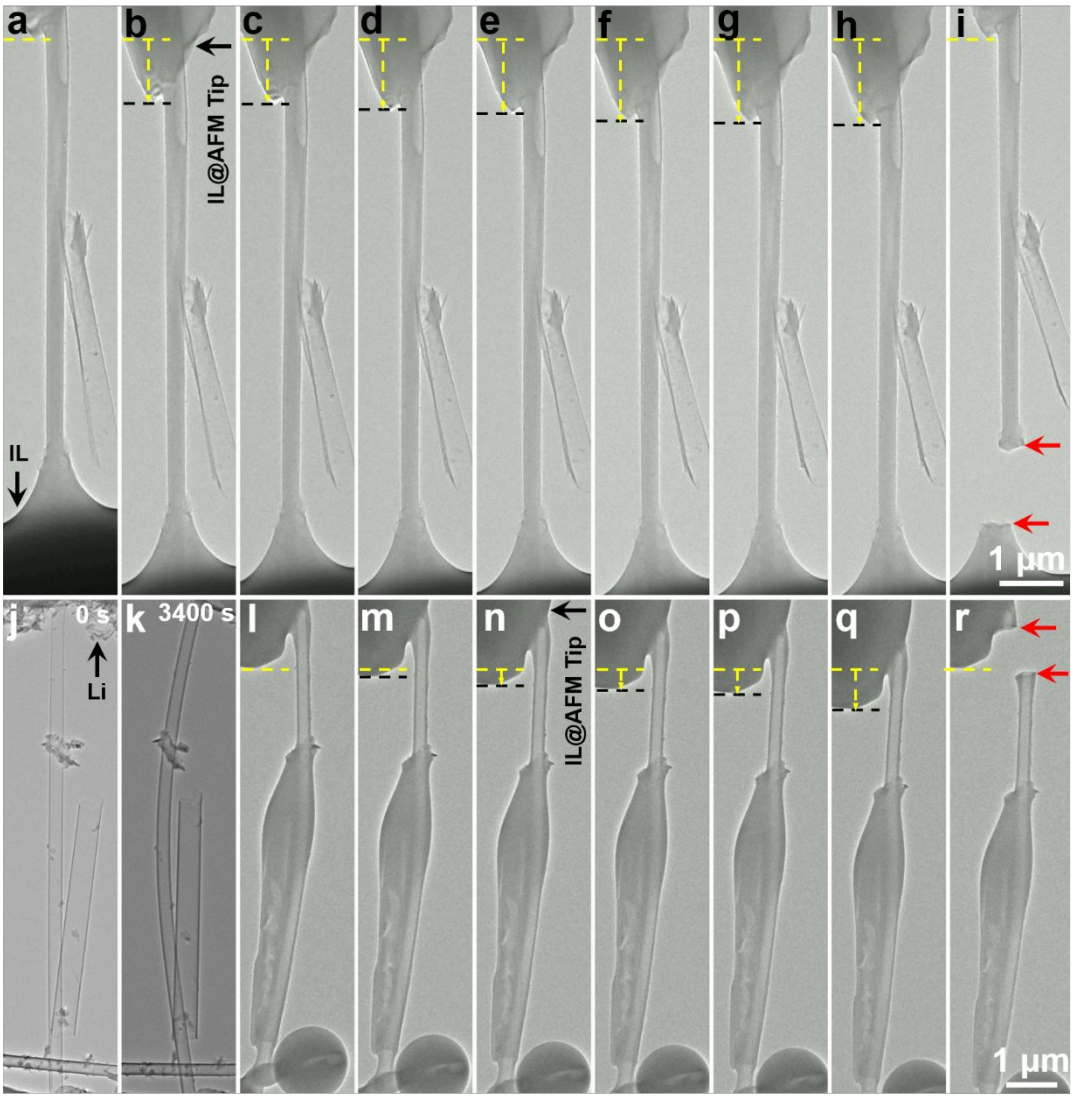

Figure S10. Tensile experiments in a pristine (a-i) and a lithiated (j-r) CNT. Both the pristine and the lithiated CNTs exhibit brittle fracture showing a sharp fracture surface (red arrows) perpendicular to the longitudinal direction of the CNT (i, r).

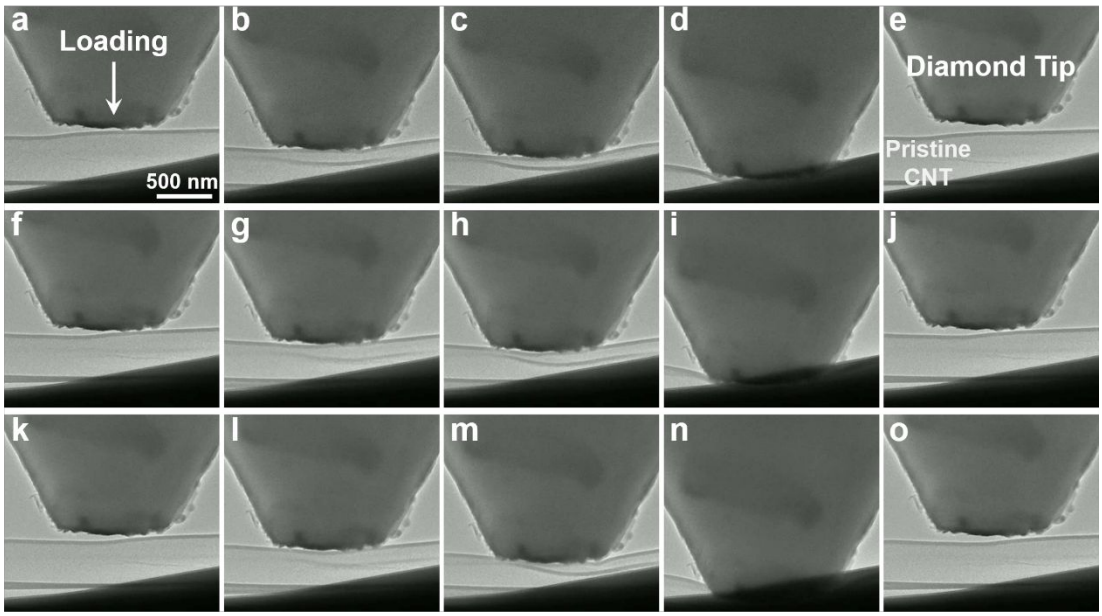

Figure S11. Three cycles of compression and unloading of a pristine CNT. Note the CNT always resumes to its initial shape after unloading (e, j, o).

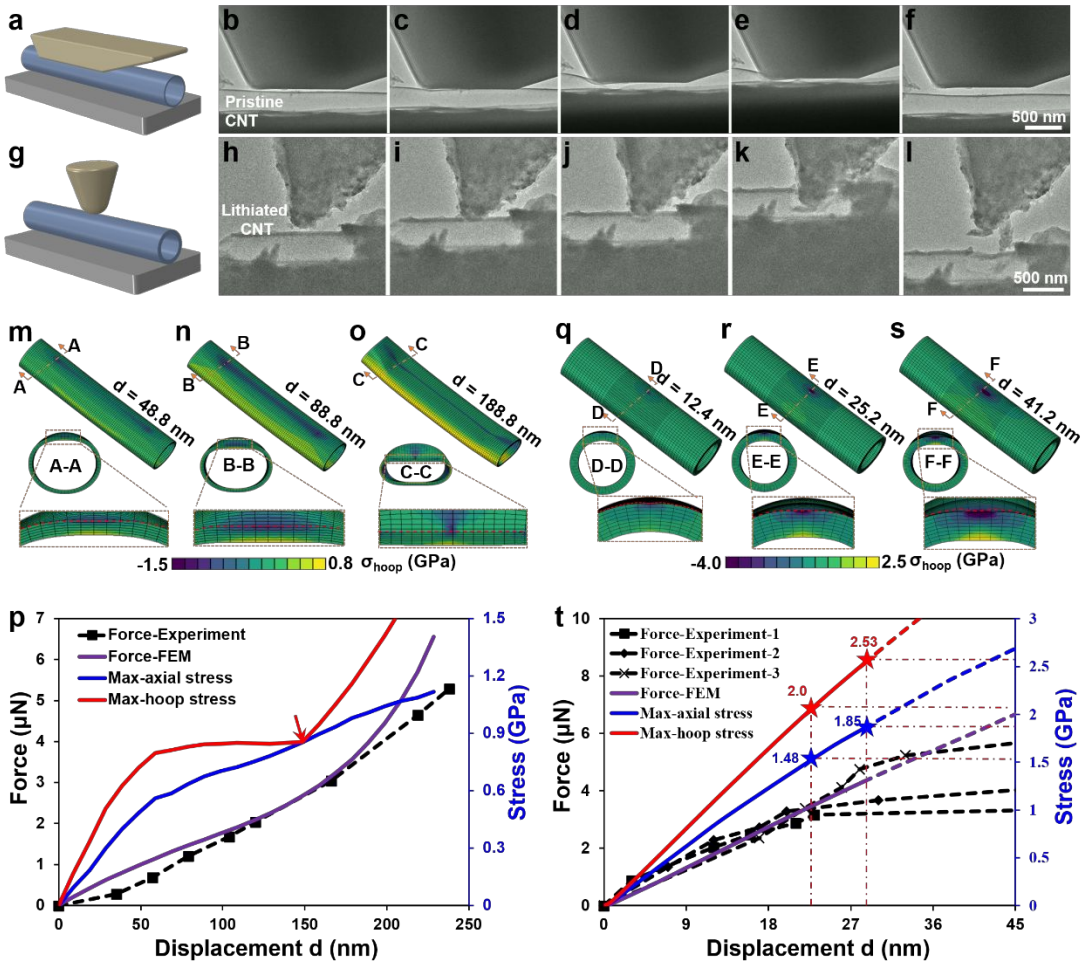

Figure S12. Radial compression of a pristine (a-f, m-p) and a lithiated (g-l, q-t) CNT. (a, g) Schematics of the experimental configurations for the compression of the pristine and the lithiated CNT, respectively. (b-f, h-l) Sequential TEM images showing the compression processes of the pristine and lithiated CNTs, respectively. Note that for the pristine CNT, it resumed to its initial shape after release of stress (f), indicating good elasticity of the pristine CNT. However, the lithiated CNT exhibits brittle fracture characteristic after compression (k, l). (m-o) and (q-s) are FEM simulations to the experimental results shown in (b-f) and (h-l), respectively. Both longitudinal and cross-sectional views are provided. (p) and (t) are experimental and simulated force-displacement plots and maximum hoop and axial stress-displacement plots corresponding to (a-f, m-o) and (g-l, q-s), respectively. The inflection points in the hoop stress-displacement curve indicate a transition of the maximum stress from the center of inner part of CNT to the edges of the CNT.

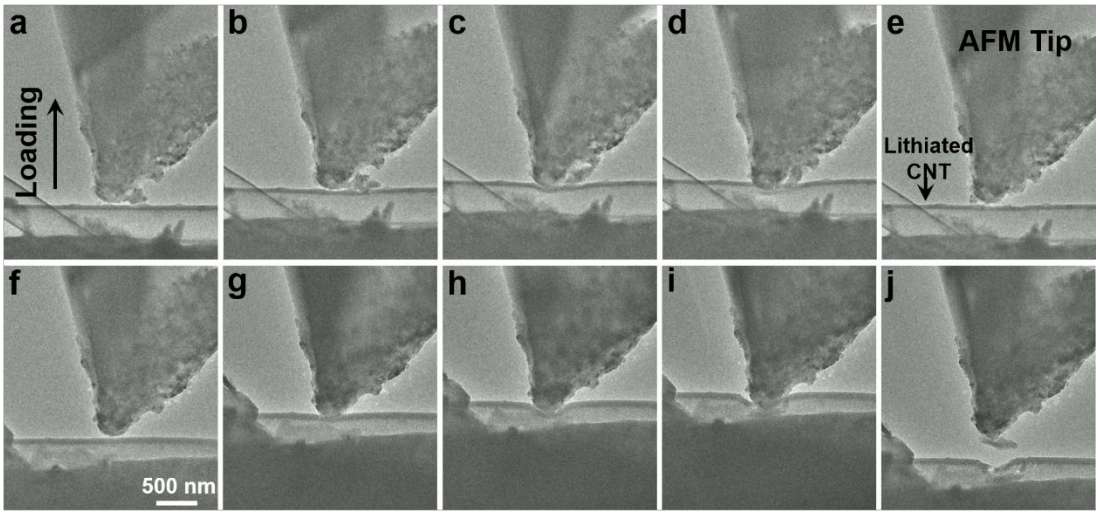

Figure S13. Two cycles of compression and unloading of a lithiated CNT. Note the CNT fractured after compression (i, j).

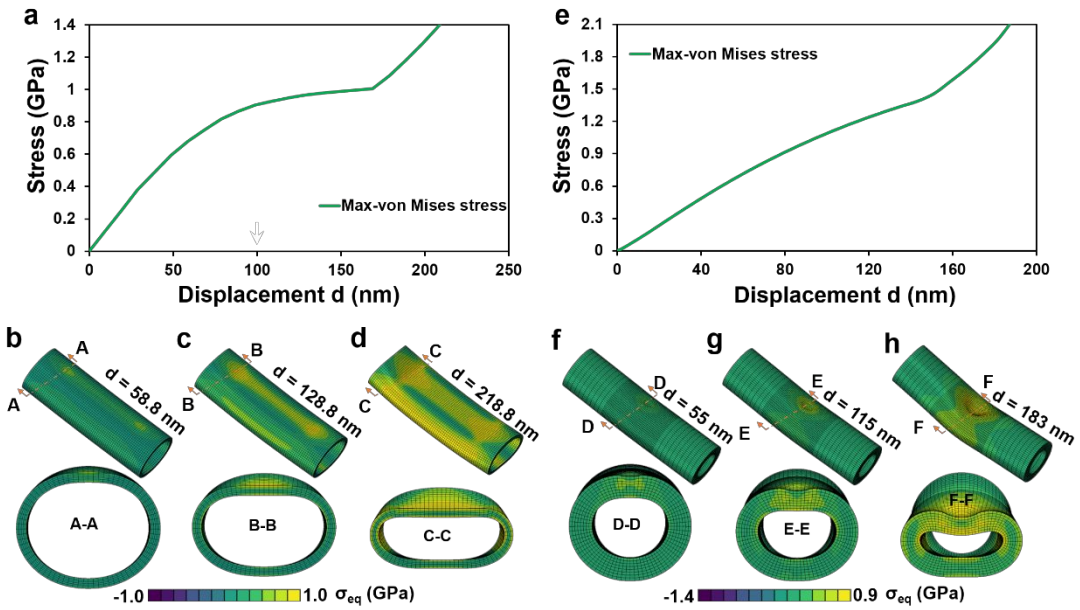

Figure S14. The maximum equivalent stress-dispalcement plots of the the pristine (a) and lithiated (e) CNTs corresponding to the model shown in **Figure 3**. The inflection points in equivalent stress-displacement curve indicate a transition of the maximum stress from the center to both edges of the CNT. (b-d) and (f-h) are the equivalent stress distribution of the pristine and the lithiated CNTs, respectively. Both longitudinal and cross-sectional views are provided.

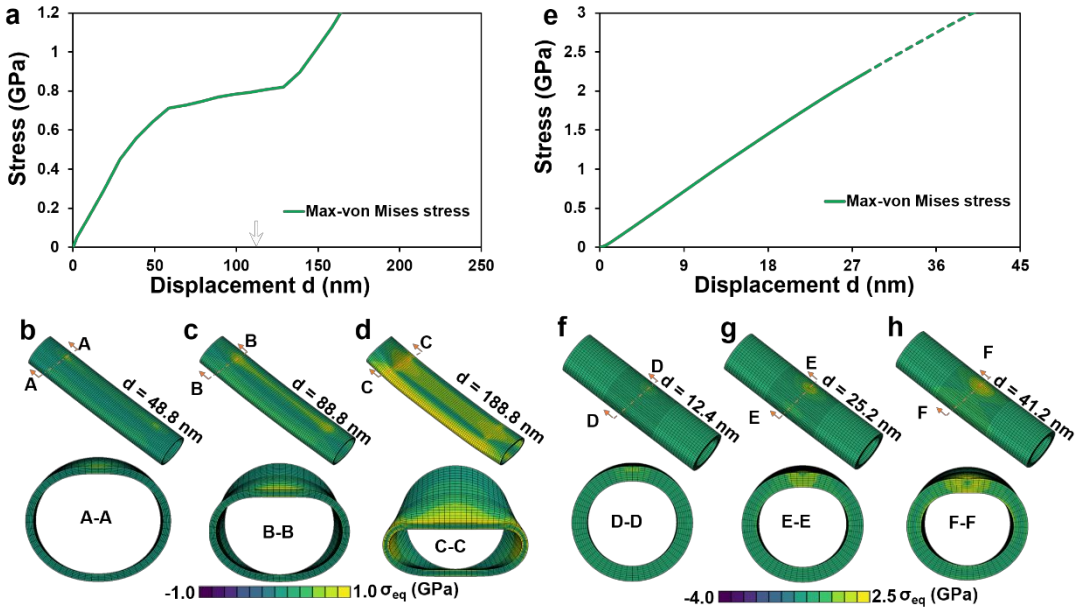

Figure S15. The maximum equivalent stress-dispalcement plots of the pristine (a) and the lithiated (e) CNTs corresponding to the model in **Figure S11**. The inflection points in equivalent stress-displacement curve indicate a transition of the maximum stress from the center to the flattened edges of the CNT. (b-d) and (f-h) are the equivalent stress distribution of the pristine and the lithiated CNTs, respectively. Both longitudinal and cross-sectional views are provided.

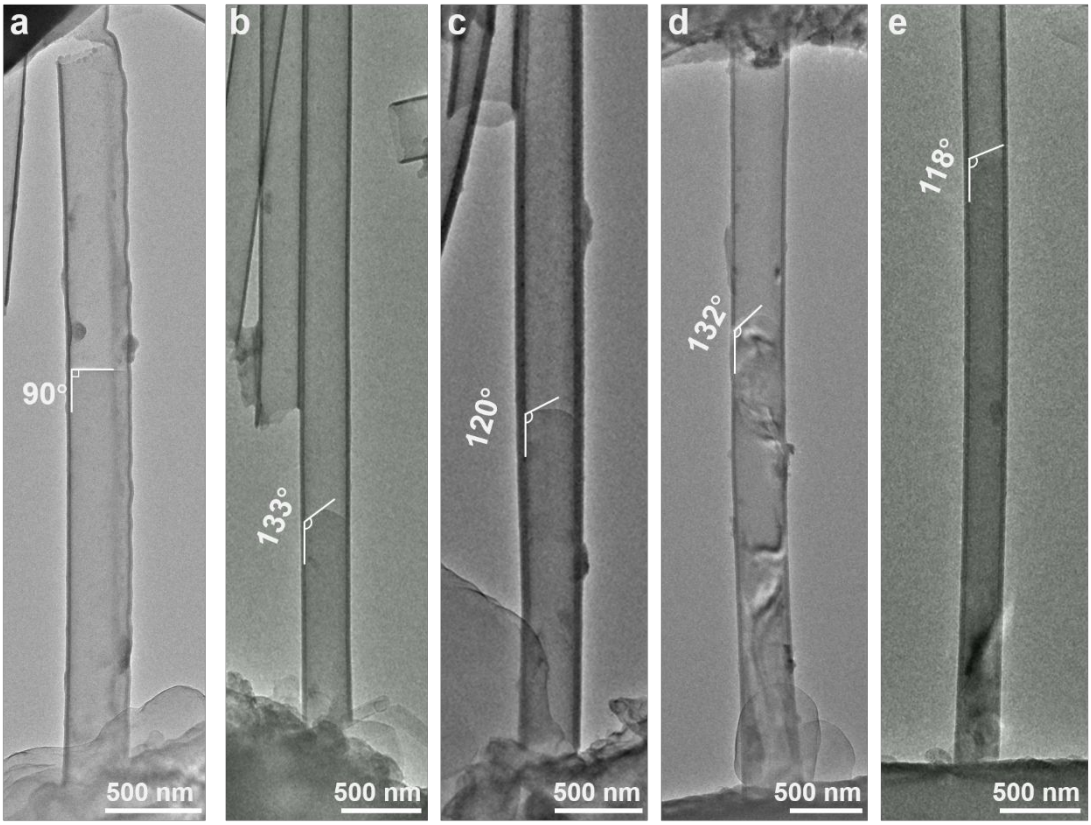

Figure S16. The contact angles measurement of Li inside CNTs under (a) vacuum, and (b-e) CO_2 ambient. The contact angle is 90° under vacuum (a). The average contact angle in four different CNTs under CO_2 ambient is 126° (b-e).

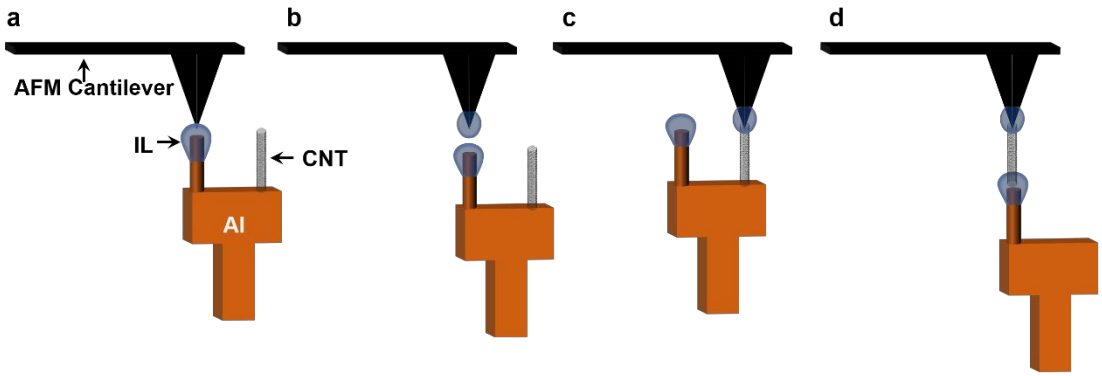

Figure S17. Schematics showing the process of welding the pristine or lithiated CNT by IL under e-beam irradiation in ETEM.

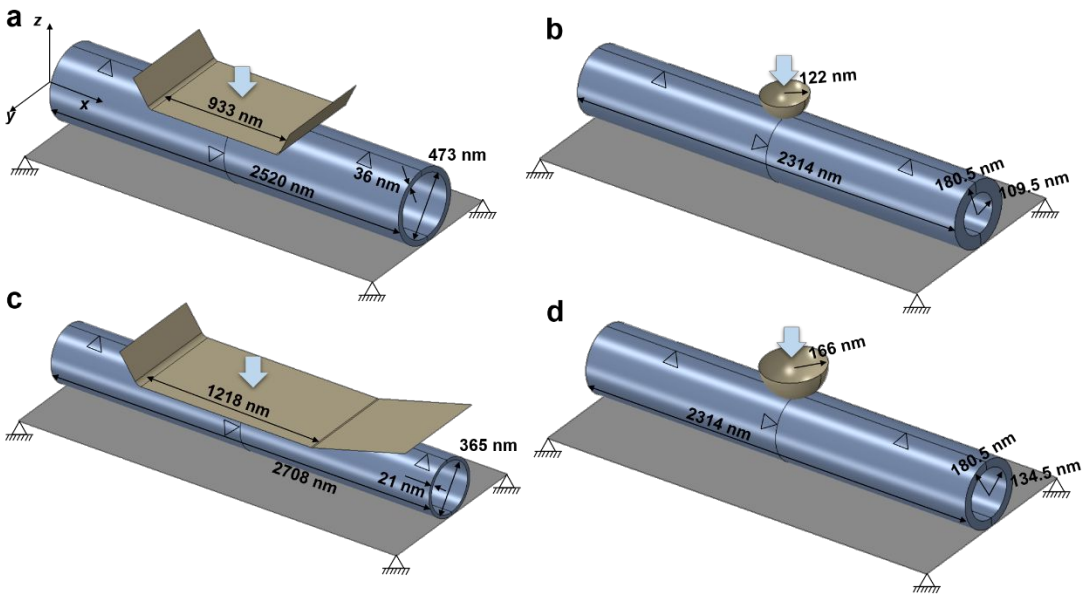

Figure S18. The models size, the boundary condition and the displacement loading conditions of the FEA simulations. (a,c) and (b,d) represent the pristine and lithiated CNTs compressed by different AFM tips , respectively.

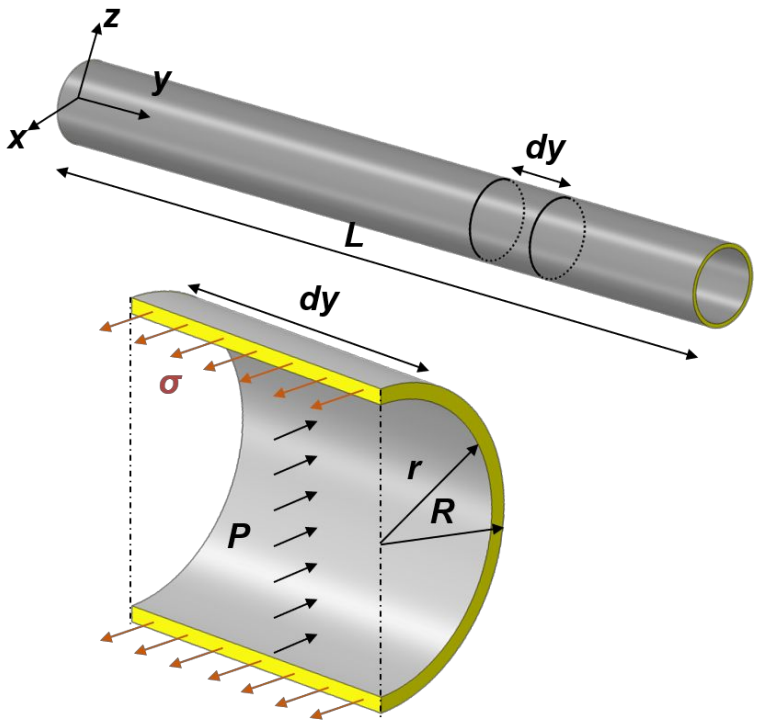

Figure S19. The model for calculating the internal pressure inside the CNTs caused by lithium deposition.

References

(1) Wang, Z.; Tang, Y.; Zhang, L.; Li, M.; Shan, Z.; Huang, J. In Situ TEM Observations of Discharging/Charging of Solid-State Lithium-Sulfur Batteries at High Temperatures. *Small* **2020,** *16*, 2001899.

(2) Chen, Y.; Wang, Z.; Li, X.; Yao, X.; Wang, C.; Li, Y.; Xue, W.; Yu, D.; Kim, S. Y.; Yang, F.; Kushima, A.; Zhang, G.; Huang, H.; Wu, N.; Mai, Y.-W.; Goodenough, J. B.; Li, J. Li metal deposition and stripping in a solid-state battery via Coble creep. *Nature* **2020,** *578*, 251-255.

(3) Zhang, L.; Yang, T.; Du, C.; Liu, Q.; Tang, Y.; Zhao, J.; Wang, B.; Chen, T.; Sun, Y.; Jia, P.; Li, H.; Geng, L.; Chen, J.; Ye, H.; Wang, Z.; Li, Y.; Sun, H.; Li, X.; Dai, Q.; Tang, Y.; Peng, Q.; Shen, T.; Zhang, S.; Zhu, T.; Huang, J. Lithium whisker growth and stress generation in an in situ atomic force microscope–environmental transmission electron microscope set-up. *Nat. Nanotechnol.* **2020,** *15*, 94-98.

(4) Yang, W.; Mao, S.; Yang, J.; Shang, T.; Song, H.; Mabon, J.; Swiech, W.; Vance, J. R.; Yue, Z.; Dillon, S. J.; Xu, H.; Xu, B. Large-deformation and high-strength amorphous porous carbon nanospheres. *Sci. Rep.* **2016,** *6*, 24187.

(5) Yang, W.; Yang, J.; Dong, Y.; Mao, S.; Gao, Z.; Yue, Z.; Dillon, S. J.; Xu, H.; Xu, B. Probing buckling and post-buckling deformation of hollow amorphous carbon nanospheres: In-situ experiment and theoretical analysis. *Carbon* **2018,** *137*, 411-418.